

# nanoCMB: A minimal CMB power spectrum calculator in Python

Adam Moss <sup>a,\*</sup>

<sup>a</sup>*School of Physics and Astronomy, University of Nottingham, Nottingham, NG7 2RD, United Kingdom*

## ARTICLE INFO

### Keywords:

Cosmic microwave background  
Power spectrum  
Boltzmann code  
Cosmological perturbation theory  
Scientific software

## ABSTRACT

We present nanoCMB, a minimal but accurate calculator for the unlensed CMB temperature and polarisation angular power spectra ( $C_{\ell}^{TT}$ ,  $C_{\ell}^{EE}$ ,  $C_{\ell}^{TE}$ ) of flat  $\Lambda$ CDM cosmologies. Written in  $\sim 1400$  lines of readable Python, the code implements the full line-of-sight integration method: RECFAST recombination, coupled Einstein–Boltzmann perturbation equations in synchronous gauge with a tight-coupling approximation, precomputed spherical Bessel function tables, and optimally constructed non-uniform grids in wavenumber and conformal time. Despite its brevity, nanoCMB achieves sub-percent agreement with CAMB across the multipole range  $2 \leq \ell \leq 2500$ , running in  $\sim 10$  seconds on a modern laptop. The entire calculation lives in a single, easily modifiable Python script, designed as a pedagogical bridge between textbook treatments and research-level Boltzmann solvers, with every approximation and numerical choice made explicit. We describe the physics, equations, and computational methods in detail, with code snippets illustrating each stage of the calculation. The code is publicly available at <https://github.com/adamoss/nanoCMB>.

## 1. Introduction

The cosmic microwave background (CMB) angular power spectrum is a cornerstone of precision cosmology. Measurements by COBE, WMAP, and Planck have determined the parameters of the  $\Lambda$ CDM model to percent-level accuracy or better [1], and upcoming experiments will push these constraints further. Computing the power spectrum from a set of cosmological parameters requires solving the coupled Einstein–Boltzmann equations through recombination and integrating the resulting source functions along the line of sight. This calculation was first implemented in COSMICS [3] and CMBFAST [16], and is now handled by the research-level codes CAMB [9] and CLASS [4], which underpin essentially all modern CMB parameter estimation [1].

These codes are impressive pieces of software, but they are also large — tens of thousands of lines of Fortran or C, with many layers of optimisation and historical conventions. For someone new to the field, they are not easy to learn from. Textbooks like Dodelson & Schmidt [6] explain the physics well, but there is a real gap between the equations on the page and a working code: choosing a gauge, setting up grids, implementing tight coupling, handling stiff ODEs, constructing source functions. These practical details matter enormously for accuracy but are rarely discussed.

nanoCMB tries to bridge this gap. It computes the unlensed  $TT$ ,  $EE$ , and  $TE$  power spectra for flat  $\Lambda$ CDM cosmologies in  $\sim 1400$  lines of Python, with sub-percent accuracy relative to CAMB. The code follows the physics directly: background  $\rightarrow$  recombination  $\rightarrow$  perturbations  $\rightarrow$  line-of-sight integration  $\rightarrow$  power spectra, all in a single file with no class hierarchies or configuration layers. Every approximation is spelled out and every numerical choice is visible.

Because everything is in one readable file, it is easy to modify. Swapping in a different recombination model, changing the tight-coupling scheme, or adding a new source term means editing a few functions rather than navigating a large package. This makes nanoCMB useful both for teaching and for quickly testing new ideas.

The closest predecessor is the pedagogical code of Callin [5], a Fortran implementation of the temperature anisotropy calculation. nanoCMB adds polarisation, full RECFAST recombination with helium, and optimised non-uniform grids, while staying in Python.

We restrict ourselves to unlensed scalar modes in flat cosmologies with massless neutrinos and  $w = -1$ . There is no lensing, no tensors, no massive neutrinos, no curvature, and no isocurvature modes. These limitations keep the code short; the modular structure should make extensions reasonably straightforward.

The remainder of this paper follows the structure of the code itself. Section 2 describes the background cosmology. Section 3 covers recombination and the ionisation history. Section 4 presents the Boltzmann hierarchy and its numerical solution. Section 5 describes the line-of-sight integration method. Section 6 covers the power spectrum assembly. Section 7 discusses the optimal non-uniform grid construction. Section 8 validates the final power spectra against CAMB. Section 9 concludes. The code is publicly available at <https://github.com/adamoss/nanoCMB>.

## 2. Background cosmology

### 2.1. The Friedmann equation

We work in conformal time  $\tau$  with the flat FRW metric  $ds^2 = a^2(\tau)(-d\tau^2 + d\mathbf{x}^2)$ , in units where  $c = 1$  and distances are measured in Mpc. The Hubble parameter is defined as usual with respect to cosmic time  $t$ ,

$$H \equiv \frac{1}{a} \frac{da}{dt} = \frac{\dot{a}}{a^2}, \quad H^2 = \frac{8\pi G}{3} \rho_{\text{tot}}, \quad (1)$$

\*Corresponding author

 [adam.moss@nottingham.ac.uk](mailto:adam.moss@nottingham.ac.uk) (A. Moss )

ORCID(s):

where overdots denote derivatives with respect to conformal time ( $\dot{a} \equiv da/d\tau = a^2 H$ ), and  $\rho_{\text{tot}}$  is the total energy density.

Following CAMB convention, we define the ‘‘grhoa2’’ combination

$$\mathcal{G}(a) \equiv 8\pi G \rho_{\text{tot}} a^4 = \bar{\rho}_\gamma + \bar{\rho}_\nu + (\bar{\rho}_c + \bar{\rho}_b) a + \bar{\rho}_\Lambda a^4, \quad (2)$$

where  $\bar{\rho}_i$  are the present-day density values. The Hubble parameter and conformal time derivative are then

$$H(a) = \frac{\sqrt{\mathcal{G}(a)/3}}{a^2}, \quad \frac{d\tau}{da} = \sqrt{\frac{3}{\mathcal{G}(a)}}. \quad (3)$$

In the code, these are implemented concisely:

Listing 1: Friedmann equation building blocks.

```

1 def grhoa2(a, bg):
2     """Total 8piG*rho*a^4."""
3     return (bg["grhog"] + bg["grhornomass"]
4           + (bg["grhoc"] + bg["grhob"]) * a
5           + bg["grhov"] * a**4)
6
7 def dtauda(a, bg):
8     """d(tau)/da = 1/(a^2 H) = sqrt(3/grhoa2) in Mpc."""
9     return np.sqrt(3.0 / grhoa2(a, bg))
    
```

The individual density parameters are computed from the input cosmological parameters (table 1). The photon density is derived from the CMB temperature  $T_{\text{CMB}}$  via  $\rho_\gamma = (4\sigma_{\text{SB}}/c) T_{\text{CMB}}^4$ , and the massless neutrino follows from the standard relation  $\rho_\nu = (7/8)(4/11)^{4/3} N_{\text{eff}} \rho_\gamma$ . The cosmological constant is fixed by the flatness condition  $\Omega_\Lambda = 1 - \Omega_m - \Omega_r$ .

## 2.2. Conformal time and the sound horizon

The conformal time is obtained by direct numerical integration:

$$\tau(a) = \int_0^a \frac{da'}{a'^2 H(a')} = \int_0^a \sqrt{\frac{3}{\mathcal{G}(a')}} da'. \quad (4)$$

The age of the universe in conformal time,  $\tau_0 = \tau(a = 1)$ , and the conformal time at matter–radiation equality,  $\tau_{\text{eq}}$ , are key derived quantities.

The comoving sound horizon in the photon–baryon fluid is

$$r_s(a) = \int_0^a \frac{c_s da'}{a'^2 H(a')}, \quad c_s^2 = \frac{1}{3(1+R)}, \quad (5)$$

where  $R = 3\rho_b/(4\rho_\gamma) = (3\bar{\rho}_b a)/(4\bar{\rho}_\gamma)$  is the baryon loading. The sound horizon at recombination,  $r_s(a_*)$ , sets the angular scale of the acoustic peaks via  $\theta_* = r_s/D_A(z_*)$ .

Listing 2: Sound horizon integrand.

```

1 def sound_horizon(a, bg):
2     """Comoving sound horizon r_s(a) = int_0^a c_s da'/(a'^2 H)."""
3
4     def integrand(ap):
5         R = 0.75 * bg["grhob"] * ap / bg["grhog"]
6         return 1.0 / np.sqrt(grhoa2(ap, bg) * (1.0 + R))
7     return integrate.quad(integrand, 0, a)[0]
    
```

Parameter	Symbol	Value
Baryon density	$\omega_b \equiv \Omega_b h^2$	0.02237
CDM density	$\omega_c \equiv \Omega_c h^2$	0.1200
Hubble parameter	$h$	0.6736
Scalar spectral index	$n_s$	0.9649
Scalar amplitude	$A_s$	$2.1 \times 10^{-9}$
Reionisation optical depth	$\tau_{\text{reion}}$	0.0544
Effective neutrino number	$N_{\text{eff}}$	3.044
CMB temperature	$T_{\text{CMB}}$	2.7255 K
Helium fraction	$Y_{\text{He}}$	0.245
Pivot scale	$k_0$	$0.05 \text{ Mpc}^{-1}$

Table 1

Cosmological parameters used throughout this work, corresponding to the Planck 2018 best-fit  $\Lambda$ CDM model [1].

Figure 1 compares the Hubble parameter  $H(z)$  from nanoCMB to CAMB, demonstrating agreement at the  $10^{-4}$  level across all redshifts.

## 2.3. Unit conventions

All distances are in Mpc, with  $c = 1$  so that times are also in Mpc. The Hubble parameter  $H$  has units of  $\text{Mpc}^{-1}$ , and wavenumbers  $k$  have units of  $\text{Mpc}^{-1}$ . Energy densities are stored in the CAMB convention as  $8\pi G\rho$  (units of  $\text{Mpc}^{-2}$ ), so that the Friedmann equation involves no explicit factors of  $G$ . The conversion from the conventional  $H_0 = 100 h \text{ km/s/Mpc}$  is  $H_0 = 100 h/c_{\text{km/s}}$  in code units.

## 3. Recombination

### 3.1. Physics of hydrogen recombination

As the universe cools below  $T \sim 4000 \text{ K}$ , the ionisation fraction  $x_e = n_e/n_H$  drops from unity as electrons and protons combine to form neutral hydrogen. The naïve expectation from the Saha equation is that recombination occurs at  $T \sim 3700 \text{ K}$ , but the Saha equation assumes thermal equilibrium, which fails because Lyman- $\alpha$  photons produced during recombination are immediately reabsorbed, creating a bottleneck.

The effective three-level atom model of Peebles [11] (see also Zeldovich, Kurt & Sunyaev [19]) resolves this by tracking only the ground state and the  $n = 2$  shell. Recombinations directly to the ground state produce photons that immediately ionise another atom, so the *effective* recombination rate is the case-B rate  $\alpha_B$  (to excited states only). The two escape routes from  $n = 2$  are Lyman- $\alpha$  escape (net rate suppressed by the Sobolev optical depth) and two-photon decay ( $2s \rightarrow 1s$ , rate  $\Lambda_{2s \rightarrow 1s} = 8.22 \text{ s}^{-1}$ ).

The Peebles equation for hydrogen is

$$\frac{dx_H}{dz} = \frac{C_r}{H(z)(1+z)} \left[ x_e x_H n_H \alpha_B - \beta_B (1 - x_H) e^{-E_{21}/k_B T_m} \right], \quad (6)$$

where  $x_H = n_{H^+}/n_H$  is the hydrogen ionisation fraction,  $\alpha_B$  is the case-B recombination coefficient [12],  $\beta_B =$

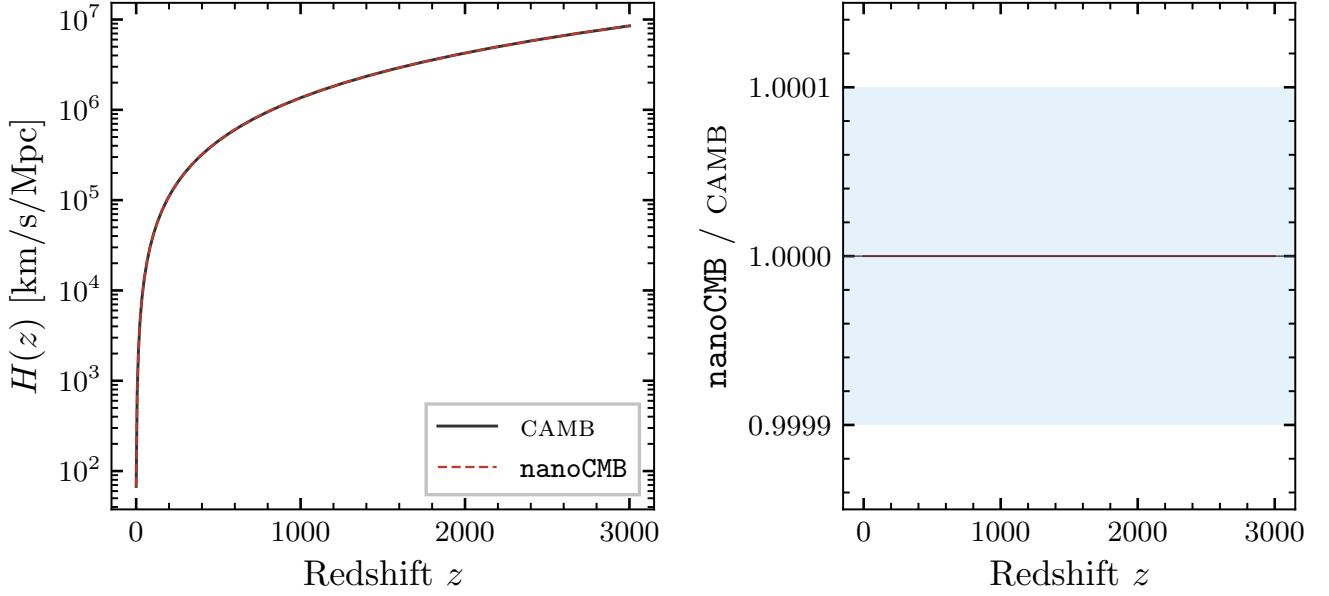


**Figure 1:** Hubble parameter comparison. *Left:*  $H(z)$  from nanoCMB (red dashed) and CAMB (black solid). *Right:* ratio, showing agreement at the  $10^{-4}$  level.

$\alpha_B (2\pi m_e k_B T_m / h^2)^{3/2} e^{-B_2/k_B T_m}$  is the photoionisation rate from  $n = 2$ ,  $E_{21}$  is the Lyman- $\alpha$  energy, and the Peebles C-factor is

$$C_r = \frac{1 + K \Lambda_{2s1s} n_{1s}}{1 + K (\Lambda_{2s1s} + \beta_B) n_{1s}}, \quad (7)$$

with  $K = \lambda_\alpha^3 / (8\pi H)$  encoding the Sobolev optical depth of the Lyman- $\alpha$  line, and  $n_{1s} = (1 - x_H) n_H$  the ground-state number density.

### 3.2. RECFAST implementation

nanoCMB implements the full RECFAST algorithm [14, 14, 15, 18], which extends the Peebles equation to include helium recombination (both He III  $\rightarrow$  He II and He II  $\rightarrow$  He I, including singlet and triplet channels with hydrogen continuum opacity corrections) and tracks the matter temperature  $T_m$  separately from the radiation temperature  $T_r = T_{\text{CMB}}(1 + z)$ .

The calculation proceeds in phases, from high to low redshift:

1.  $z > 8000$ : fully ionised ( $x_e = 1 + 2f_{\text{He}}$ , helium doubly ionised).
2.  $5000 < z < 8000$ : He<sup>++</sup>  $\rightarrow$  He<sup>+</sup> via Saha equilibrium.
3.  $3500 < z < 5000$ : He singly ionised, H fully ionised ( $x_e = 1 + f_{\text{He}}$ ).
4.  $z < 3500$ : He<sup>+</sup>  $\rightarrow$  He<sup>0</sup> in Saha equilibrium until  $x_{\text{He}} < 0.99$ , then a full three-variable ODE system ( $x_H, x_{\text{He}}, T_m$ ) solved with implicit Radau IIA, which handles the hydrogen transition automatically.

The hydrogen piece of the ODE right-hand side illustrates the Peebles equation in code:

Listing 3: Hydrogen Peebles equation from recfast\_rhs().

```

1 # Case-B recombination coefficient (Pequignot et al. 1991 fit)
2 t4 = T_mat / 1e4
3 Rdown = 1e-19 * 4.309 * t4**(-0.6166) / (1 + 0.6703 * t4**0.5300)
4 Rup = Rdown * (CR * T_mat)**1.5 * np.exp(-CDB / T_mat)
5
6 # Sobolev escape: K = lambda_alpha^3/(8pi*H) with Hswitch
7 correction
8 K = CK / Hz * (1.0
9   + AGauss1 * np.exp(-(np.log(1+z) - zGauss1) / wGauss1)**2)
10  + AGauss2 * np.exp(-(np.log(1+z) - zGauss2) / wGauss2)**2))
11 n_1s = n_H * max(1 - x_H, 1e-30)
12
13 f1 = ((x * x_H * n_H * Rdown
14       - Rup * (1 - x_H) * np.exp(-CL / T_mat))
15       * (1 + K * Lambda_2s1s * n_1s)
16       / (Hz * (1+z) * (1.0/fu + K * Lambda_2s1s * n_1s / fu
17         + K * Rup * n_1s)))
    
```

The RECFAST fudge factor  $f_u = 1.125$  and the Hswitch double-Gaussian correction to  $K$  (parameterised by amplitudes  $A_{1,2}$ , centres  $z_{1,2}$ , and widths  $w_{1,2}$ ) follow the CAMB defaults [18].

The helium singlet channel follows an analogous Peebles equation with the He I case-B coefficient of Hummer & Storey [8], Sobolev escape via the  $2^1P_1 \rightarrow 1^1S_0$  line, two-photon decay from  $2^1S_0$  (rate  $\Lambda_{\text{He}} = 51.3 \text{ s}^{-1}$ ), and hydrogen continuum opacity corrections to the effective escape probability [14, 18]. The triplet channel (He I  $2^3P_1 \rightarrow 2^3S_1$ ) provides an additional recombination pathway at  $z \gtrsim 1700$  and is included with its own Sobolev factor and continuum opacity correction.

The matter temperature  $T_m$  evolves via Compton heating/cooling against the radiation field and adiabatic expansion:

$$\frac{dT_m}{dz} = \frac{8\sigma_T a_r T_r^4}{3 H m_e c} \frac{x_e}{1 + x_e + f_{\text{He}}} (T_m - T_r) + \frac{2T_m}{1 + z}, \quad (8)$$

where  $a_r = 4\sigma_{\text{SB}}/c$  is the radiation constant. At early times the Compton timescale is much shorter than the Hubble time and  $T_m \approx T_r$ ; after decoupling, the matter cools adiabatically as  $T_m \propto (1+z)^2$  [13].

### 3.3. Reionisation

At low redshift ( $z \lesssim 10$ ), ultraviolet radiation from the first stars and galaxies reionises the intergalactic medium. We model this using the CAMB parameterisation<sup>1</sup>: a tanh transition in  $(1+z)^{3/2}$  centred on a reionisation redshift  $z_{\text{re}}$  with width  $\delta z = 0.5$ , supplemented by a second helium reionisation at  $z \approx 3.5$ .

The reionisation redshift  $z_{\text{re}}$  is not specified directly; instead, it is determined by requiring that the total reionisation optical depth matches the input parameter  $\tau_{\text{reion}}$ . We solve this implicit equation using Brent's method (`scipy.optimize.brentq`).

The final ionisation fraction is  $x_e(z) = \max[x_e^{\text{recomb}}(z), x_e^{\text{reion}}(z)]$ , ensuring a smooth transition from the recombination freeze-out to the fully reionised state.

### 3.4. Visibility function and derived quantities

The Thomson scattering opacity is

$$\dot{\kappa}(\tau) = x_e n_H \sigma_T / a^2, \quad (9)$$

where  $n_H$  is the present-day hydrogen number density and  $\sigma_T$  the Thomson cross section. The optical depth from conformal time  $\tau$  to today is

$$\tau_{\text{opt}}(\tau) = \int_{\tau}^{\tau_0} \dot{\kappa} d\tau', \quad (10)$$

and the visibility function

$$g(\tau) = \dot{\kappa} e^{-\tau_{\text{opt}}} \quad (11)$$

gives the probability that a CMB photon last scattered at conformal time  $\tau$ . Its peak defines the surface of last scattering ( $z_* \approx 1090$ ), and its width  $\Delta\tau_{\text{rec}}$  determines the thickness of the last scattering surface.

The Silk damping scale, which sets the exponential suppression of small-scale anisotropies due to photon diffusion, is

$$k_D^{-2} = \int_0^{a_*} \frac{R^2 + \frac{16}{15}(1+R)}{6(1+R)^2 \dot{\kappa}} \frac{da}{a^2 H}, \quad (12)$$

where  $R = 3\rho_b/(4\rho_\gamma)$  as before.

Figure 2 shows the ionisation history, visibility function, and opacity from nanoCMB compared to CAMB.

## 4. Perturbation theory

### 4.1. Synchronous gauge

We work in the synchronous gauge with the CDM rest-frame convention, matching CAMB [9] and following the

<sup>1</sup><https://cosmologist.info/notes/CAMB.pdf>

notation of Ma & Bertschinger [10]. The perturbed metric is

$$ds^2 = a^2(\tau) [-d\tau^2 + (\delta_{ij} + h_{ij}) dx^i dx^j], \quad (13)$$

where  $h_{ij}$  decomposes into scalar modes characterised by  $h$  and  $\eta$  in Fourier space. The key metric variable evolved in the code is  $k\eta$ , the product of the wavenumber and the synchronous-gauge metric perturbation  $\eta$ .

The Einstein constraint equations determine the gravitational potentials from the matter perturbations:

$$h/2 = -kz, \quad z = \frac{\delta\rho/(2k) + k\eta}{\dot{a}/a}, \quad (14)$$

$$\sigma = z + \frac{3}{2} \frac{\delta q}{k^2}, \quad (15)$$

where  $\delta\rho$  and  $\delta q$  are the total density and momentum perturbations, and  $\sigma = (\dot{h} + 6\dot{\eta})/(2k)$  is the shear.

### 4.2. Boltzmann hierarchy

The distribution function for each species is expanded in Legendre multipoles. We describe the evolution equations for each species in turn.

#### 4.2.1. Photons

The photon density perturbation  $\delta_\gamma = \Theta_0$  and momentum perturbation  $q_\gamma = (4/3)\Theta_1$  evolve as

$$\dot{\delta}_\gamma = -k \left( \frac{4}{3} z + q_\gamma \right), \quad (16)$$

$$\dot{q}_\gamma = \frac{k}{3} (\delta_\gamma - 2\pi_\gamma) + \dot{\kappa} \left( \frac{4}{3} v_b - q_\gamma \right), \quad (17)$$

where  $\pi_\gamma = \Theta_2$  is the photon anisotropic stress and the Thomson scattering term in  $\dot{q}_\gamma$  couples the photon and baryon momenta. The higher multipoles ( $\ell \geq 2$ ) obey

$$\begin{aligned} \dot{\Theta}_\ell = \frac{k}{2\ell+1} & \left[ \ell \Theta_{\ell-1} - (\ell+1) \Theta_{\ell+1} \right] + \delta_{\ell 2} \frac{8}{15} k \sigma \\ & - \dot{\kappa} \left[ \Theta_\ell - \delta_{\ell 0} \Theta_0 - \delta_{\ell 1} v_b - \delta_{\ell 2} \Pi \right], \end{aligned} \quad (18)$$

where  $\Pi = \Theta_2/10 + 3E_2/5$  is the polarisation source.

The photon polarisation hierarchy ( $\ell \geq 2$ ) is

$$\begin{aligned} \dot{E}_\ell = \frac{k}{2\ell+1} & \left[ \ell E_{\ell-1} - \frac{(\ell+3)(\ell-1)}{\ell+1} E_{\ell+1} \right] \\ & - \dot{\kappa} \left[ E_\ell - \delta_{\ell 2} \Pi \right]. \end{aligned} \quad (19)$$

Thomson scattering couples the temperature quadrupole  $\Theta_2$  and the polarisation quadrupole  $E_2$  through  $\Pi$ , generating E-mode polarisation from the photon anisotropy at the last scattering surface.

#### 4.2.2. Massless neutrinos

Massless neutrinos free-stream after decoupling at  $T \sim 1$  MeV and obey an unscattered Boltzmann hierarchy. The monopole and dipole are

$$\dot{\delta}_\nu = -k \left( \frac{4}{3} z + q_\nu \right), \quad (20)$$

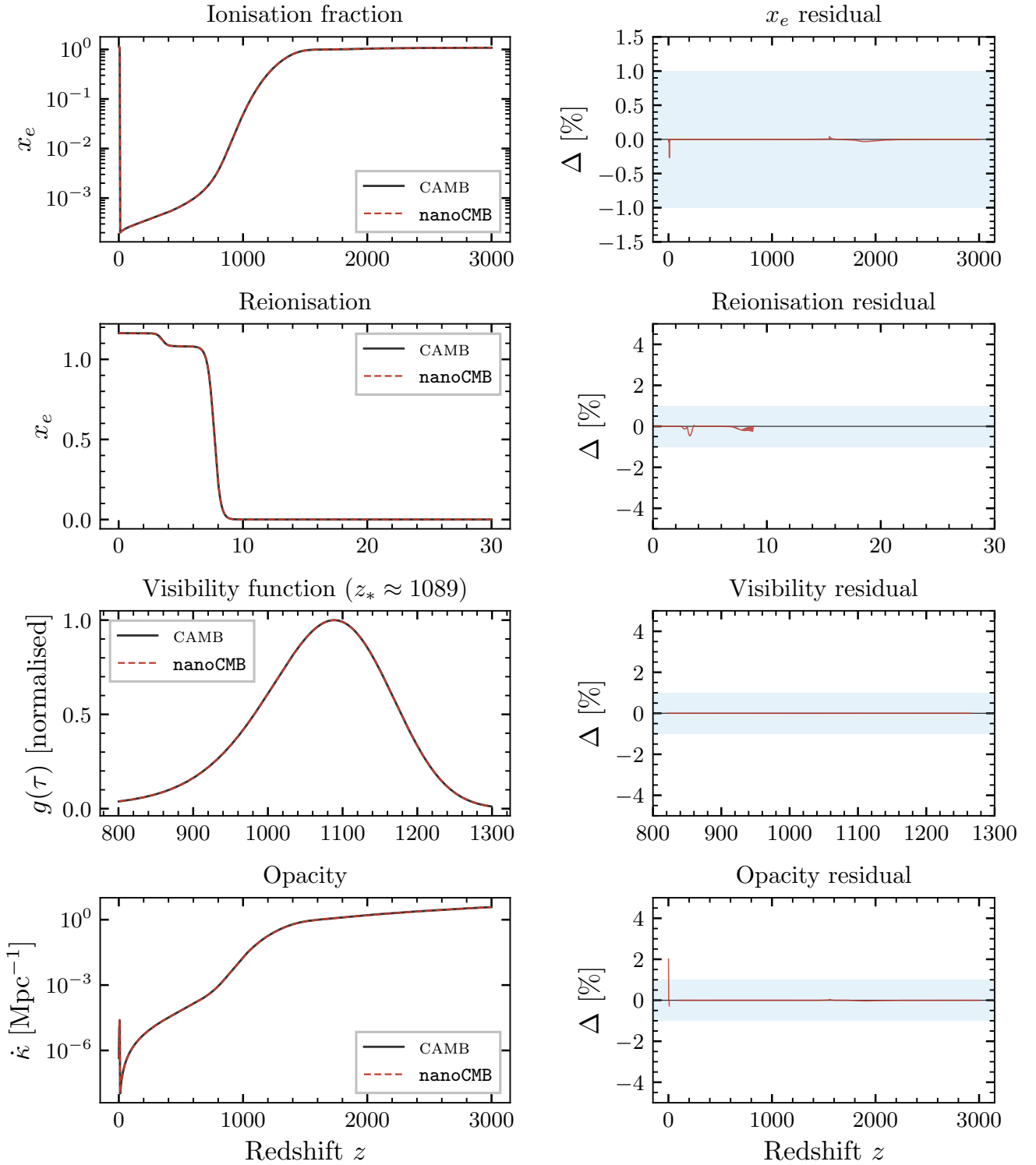


**Figure 2:** Thermodynamic quantities from nanoCMB (red dashed) compared to CAMB (black solid). *Top row:* ionisation fraction  $x_e(z)$ . *Second row:* reionisation window at  $z < 30$ . *Third row:* visibility function near recombination. *Bottom row:* Thomson opacity  $\dot{\kappa}$ . Right panels show ratios, demonstrating sub-percent agreement.

$$\dot{q}_\nu = \frac{k}{3} (\delta_\nu - 2\pi_\nu), \quad (21)$$

where  $q_\nu = (4/3)\mathcal{N}_1$  is the neutrino momentum perturbation and  $\pi_\nu = \mathcal{N}_2$  the anisotropic stress. The higher multipoles ( $\ell \geq 2$ ) obey

$$\dot{\mathcal{N}}_\ell = \frac{k}{2\ell + 1} [\ell \mathcal{N}_{\ell-1} - (\ell + 1) \mathcal{N}_{\ell+1}] + \delta_{\ell 2} \frac{8}{15} k \sigma. \quad (22)$$

The  $\ell = 2$  source term from the metric shear  $\sigma$  seeds the neutrino anisotropic stress, which in turn affects the gravitational potentials through the Einstein equations. Unlike photons, there is no scattering term, so all multipoles are populated by free streaming.

#### 4.2.3. Cold dark matter

In the synchronous gauge with the CDM at rest, the CDM equations are simply

$$\dot{\delta}_c = -kz, \quad (23)$$

and the CDM velocity is zero by gauge choice. CDM is pressureless and collisionless, so it has no higher multipoles.

#### 4.2.4. Baryons

The baryon density and velocity evolve as

$$\dot{\delta}_b = -k(z + v_b), \quad (24)$$

$$\dot{v}_b = -\frac{\dot{a}}{a} v_b + k c_{s,b}^2 \delta_b - \frac{\dot{k} \bar{\rho}_\gamma}{a \bar{\rho}_b} \left( \frac{4}{3} v_b - q_\gamma \right), \quad (25)$$

where the last term in the velocity equation is the Thomson drag force coupling baryons to photons. The baryon sound speed is

$$c_{s,b}^2 = \frac{k_B T_m}{\mu m_H} \left( 1 - \frac{1}{3} \frac{d \ln T_m}{d \ln a} \right), \quad (26)$$

with  $\mu^{-1} = 1 - \frac{3}{4} Y_{\text{He}} + (1 - Y_{\text{He}}) x_e$  the inverse mean molecular weight in units of  $m_H$ . At early times, Compton scattering keeps  $T_m \approx T_r \propto 1/a$  so that  $c_{s,b}^2 = (4/3) k_B T_m / (\mu m_H)$ ; after decoupling,  $T_m \propto a^{-2}$  (adiabatic cooling) and the factor approaches  $5/3$ . This thermal pressure term is a small correction but is included for consistency with CAMB.

The state vector is laid out as a flat array for the SciPy ODE solver:

Listing 4: State vector index layout.

```

1 LMAXG = 15      # photon temperature: Theta_0 ... Theta_LMAXG
2 LMAXPOL = 15   # photon polarisation: E_2 ... E_LMAXPOL
3 LMAXNR = 15   # massless neutrinos: N_0 ... N_LMAXNR
4
5 IX_ETAK = 0    # k*eta (metric)
6 IX_CLXC = 1    # delta_c (CDM density)
7 IX_CLXB = 2    # delta_b (baryon density)
8 IX_VB = 3     # v_b (baryon velocity)
9 IX_G = 4      # Theta_0, Theta_1, ...
10 IX_POL = IX_G + LMAXG + 1 # E_2, E_3, ...
11 IX_R = IX_POL + LMAXPOL - 1 # N_0, N_1, ...
12 NVAR = IX_R + LMAXNR + 1   # total: 50 variables
    
```

### 4.3. Tight-coupling approximation

At early times when the photon mean free path is much smaller than the wavelength of the perturbation ( $k/\dot{k} \ll 1$ ) and the Hubble time ( $1/(\dot{k}\tau) \ll 1$ ), the photon–baryon system is tightly coupled and the higher photon multipoles are exponentially suppressed. In this regime, evolving the full hierarchy is both unnecessary and numerically stiff.

In tight coupling, the photon–baryon system is treated as a single fluid, with the photon quadrupole determined algebraically from the shear:

$$\Theta_2^{\text{TC}} = \frac{32}{45} \frac{k}{\dot{k}} (\sigma + v_b), \quad (27)$$

and the baryon velocity equation becomes

$$\dot{v}_b = \frac{-\frac{\dot{a}}{a} v_b + k c_{s,b}^2 \delta_b + \frac{k}{4} \frac{4\rho_\gamma}{3\rho_b} (\Theta_0 - 2\Theta_2^{\text{TC}})}{1 + \frac{4\rho_\gamma}{3\rho_b}}. \quad (28)$$

This approximation reduces the stiffness of the system and allows the ODE solver to take much larger time steps during the tightly-coupled era. The transition criterion is  $\max(k/\dot{k}, 1/(\dot{k}\tau)) < 0.01$ .

### 4.4. Adiabatic initial conditions

The perturbations are initialised deep in the radiation era when  $k\tau \ll 1$ , using the standard adiabatic growing mode [10]. The leading-order terms are:

$$k\eta = -k \left( 1 - \frac{(k\tau)^2}{12} \left( 1 - \frac{10}{4R_\nu + 15} \right) \right), \quad (29)$$

$$\delta_\gamma = \delta_\nu = \frac{(k\tau)^2}{3}, \quad \delta_c = \delta_b = \frac{3}{4} \delta_\gamma, \quad (30)$$

where  $R_\nu = \rho_\nu / (\rho_\nu + \rho_\gamma)$  is the neutrino fraction of the radiation density. The photon and baryon velocities start at  $(3/4)q_\gamma$ , and the neutrino anisotropic stress is seeded at second order in  $k\tau$ :

$$\pi_\nu = -\frac{4}{3} \frac{(k\tau)^2}{4R_\nu + 15}. \quad (31)$$

Listing 5: Adiabatic initial conditions (excerpt).

```

1 x = k * tau; x2 = x * x
2 Rv = bg["grhornomass"] / grho_rad # neutrino fraction
3 Rp15 = 4 * Rv + 15
4
5 y0[IX_ETAK] = -k * (1.0 - x2/12.0 * (-10.0/Rp15 + 1.0))
6 clxg_init = x2 / 3.0
7 y0[IX_G] = clxg_init # delta_gamma
8 y0[IX_CLXC] = 0.75 * clxg_init # delta_c = (3/4)*delta_gamma
9 y0[IX_CLXB] = 0.75 * clxg_init # delta_b
10 y0[IX_R] = clxg_init # delta_nu = delta_gamma
11 y0[IX_R + 2] = -4.0/3.0 * x2 / Rp15 # pi_nu
    
```

### 4.5. Hierarchy truncation

The Boltzmann hierarchy is formally infinite. We truncate at  $\ell_{\text{max}} = 15$  for all species, using the free-streaming

closure relation for the highest multipole:

$$\dot{\Theta}_{\ell_{\max}} = k \Theta_{\ell_{\max}-1} - \frac{\ell_{\max} + 1}{\tau} \Theta_{\ell_{\max}} - \dot{k} \Theta_{\ell_{\max}}, \quad (32)$$

where the  $(\ell_{\max} + 1)/\tau$  term approximates the coupling to the unresolved  $\ell_{\max} + 1$  mode using the free-streaming relation for a plane wave. The same closure is used for neutrinos (without the scattering term).

The perturbation evolution is carried out using SciPy's LSODA integrator, which automatically switches between the non-stiff Adams method and the stiff BDF method as needed. This is well-suited to the transition from tight coupling to free streaming.

Figure 3 shows the evolution of all perturbation variables at  $k = 0.05 \text{ Mpc}^{-1}$ , compared to CAMB.

## 5. Source functions and line-of-sight integration

### 5.1. The formal line-of-sight integral

Rather than tracking the full photon distribution to each multipole  $\ell$  up to  $\ell_{\max} \sim 2500$ , we use the line-of-sight (LOS) integration method of Seljak & Zaldarriaga [16]. The transfer function at multipole  $\ell$  for wavenumber  $k$  is

$$\Delta_{\ell}^T(k) = \int_0^{\tau_0} S_T(k, \tau) j_{\ell}(k\chi) d\tau, \quad (33)$$

where  $\chi = \tau_0 - \tau$  is the comoving distance and  $j_{\ell}$  is the spherical Bessel function. The source function  $S_T$  encodes the photon monopole, dipole, and quadrupole contributions, weighted by the visibility function and its derivatives.

### 5.2. Integration by parts decomposition

The raw source function involves derivatives of the visibility function  $g(\tau)$ , which are numerically noisy. CAMB handles this by computing the visibility derivatives  $\dot{g}$  and  $\ddot{g}$  directly and folding them into a single composite source multiplied by  $j_{\ell}$ . We take the alternative approach of integrating by parts to transfer these derivatives onto the smooth Bessel functions, decomposing the temperature transfer into three channels:

$$\Delta_{\ell}^T(k) = \int d\tau [S_0 j_{\ell}(k\chi) + S_1 j'_{\ell}(k\chi) + S_2 j''_{\ell}(k\chi)], \quad (34)$$

where the three source terms are:

$$S_0 = 2\dot{\Phi} e^{-\tau_{\text{opt}}} + g \left( -\eta + 2\Phi + \frac{\Theta_0}{4} + \frac{5}{8}\Pi \right), \quad (35)$$

$$S_1 = g(\sigma + v_b), \quad (36)$$

$$S_2 = \frac{15}{8} g \Pi. \quad (37)$$

The gravitational potential  $\Phi$  is determined by the Einstein constraint

$$\Phi = -\frac{\delta\rho + 3(\dot{a}/a)\delta q/k + \delta\pi}{2k^2}, \quad (38)$$

and its time derivative  $\dot{\Phi}$  (the ISW source) is computed from the perturbed Einstein equations.

The E-mode polarisation transfer function uses a simpler form:

$$\Delta_{\ell}^E(k) = \int d\tau \frac{15}{8} \frac{g \Pi}{\chi^2 k^2} j_{\ell}(k\chi). \quad (39)$$

In the code, the three temperature source channels are assembled as:

Listing 6: Source function assembly (IBP decomposition).

```
1 src_j0 = ISW_arr + vis_arr * (monopole_arr + 0.625 * polter_arr)
2 src_j1 = vis_arr * sigma_plus_vb_arr
3 src_j2 = 1.875 * vis_arr * polter_arr
```

### 5.3. Gravitational potentials and the ISW effect

The integrated Sachs–Wolfe (ISW) effect arises from the time derivative of the gravitational potential  $\dot{\Phi}$ . This is non-zero during the radiation-to-matter transition (early ISW, which boosts the first acoustic peak) and during dark energy domination at late times (late ISW, which affects low  $\ell$ ).

Computing  $\dot{\Phi}$  requires the time derivatives of the photon and neutrino anisotropic stresses  $\dot{\pi}_{\gamma}$  and  $\dot{\pi}_{\nu}$ , which we obtain directly from the Boltzmann hierarchy equations rather than by numerical differentiation:

$$\dot{\Phi} = \frac{1}{2k^2} \left[ \frac{\dot{a}}{a} (-\delta\pi - 2k^2\Phi) + k\delta q - \delta\dot{\pi} + k\sigma(\bar{\rho}_{\text{tot}} + \bar{P}_{\text{tot}}) \right], \quad (40)$$

where  $\delta\dot{\pi} = \bar{\rho}_{\gamma} \dot{\pi}_{\gamma} + \bar{\rho}_{\nu} \dot{\pi}_{\nu} - 4(\dot{a}/a)\delta\pi$ .

### 5.4. Precomputed Bessel function tables

The spherical Bessel functions  $j_{\ell}(x)$  are needed at millions of points during the LOS integration. We precompute them on a uniform  $x$ -grid with spacing  $\Delta x = 0.03$ , then interpolate linearly during integration. Several optimisations are employed:

- *Dead-zone skipping*: For large  $\ell$ ,  $j_{\ell}(x)$  is exponentially small for  $x < \ell - O(\ell^{1/3})$ . We skip this region during both evaluation and integration.
- *Bessel derivatives by recurrence*: Rather than computing  $j'_{\ell}$  and  $j''_{\ell}$  independently, we use the standard recurrence relations:

$$j'_{\ell}(x) = \frac{\ell}{x} j_{\ell}(x) - j_{\ell+1}(x), \quad (41)$$

$$j''_{\ell}(x) = -\frac{2}{x} j'_{\ell}(x) + \left[ \frac{\ell(\ell+1)}{x^2} - 1 \right] j_{\ell}(x), \quad (42)$$

which require only  $j_{\ell}$  and  $j_{\ell+1}$  (both already tabulated).

- *Disk caching*: Bessel tables are cached to disk (keyed by a hash of the  $\ell$ -values and grid parameters), so subsequent runs skip the expensive evaluation entirely.

Perturbation evolution at  $k = 0.05 \text{ Mpc}^{-1}$

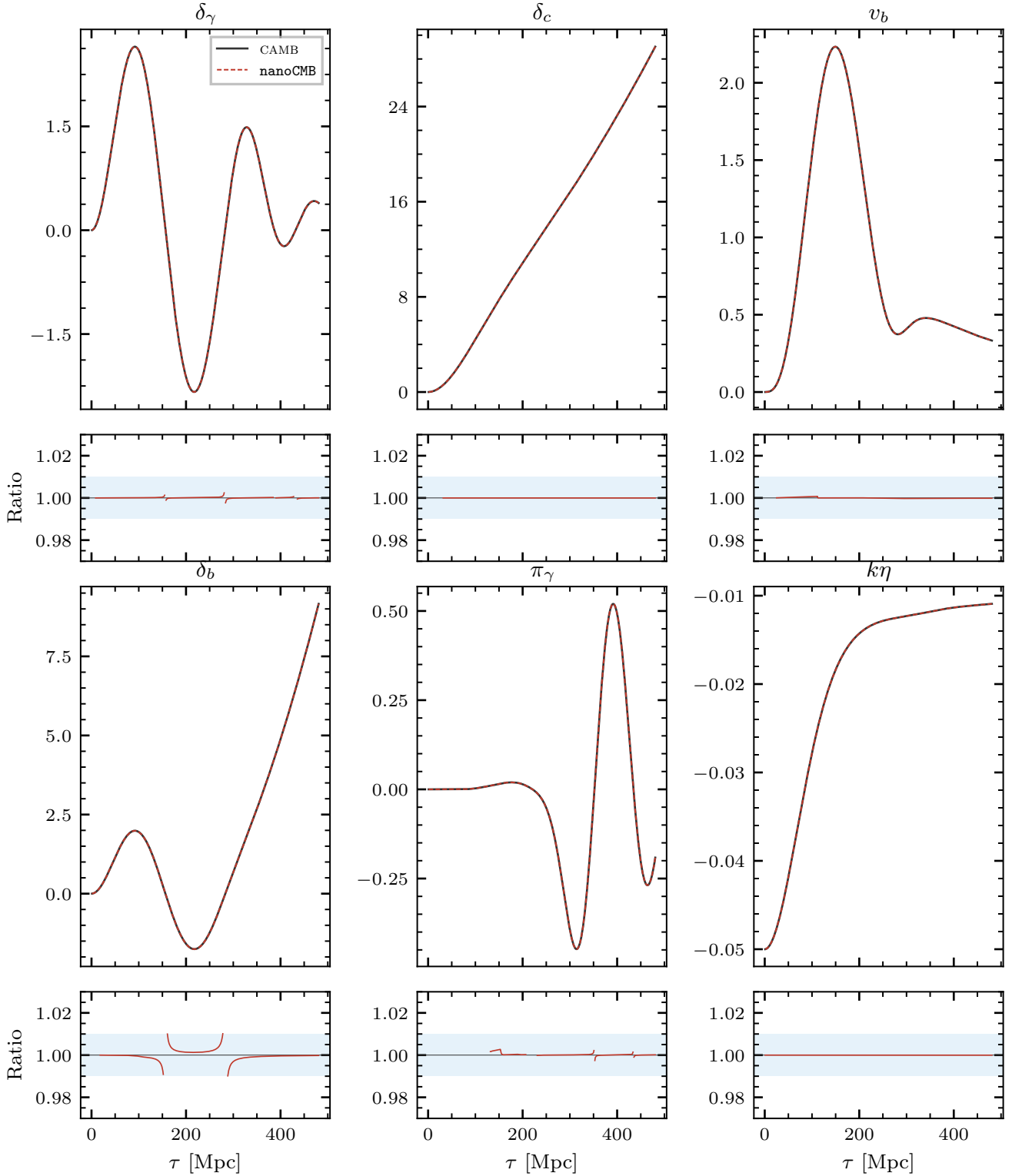


**Figure 3:** Perturbation evolution at  $k = 0.05 \text{ Mpc}^{-1}$ . Top panels show  $\delta_\gamma$ ,  $\delta_c$ ,  $v_b$ ,  $\delta_b$ ,  $\pi_\gamma$ , and  $k\eta$  from nanoCMB (red dashed) and CAMB (black solid). Bottom panels show ratios, with the  $\pm 1\%$  band shaded.

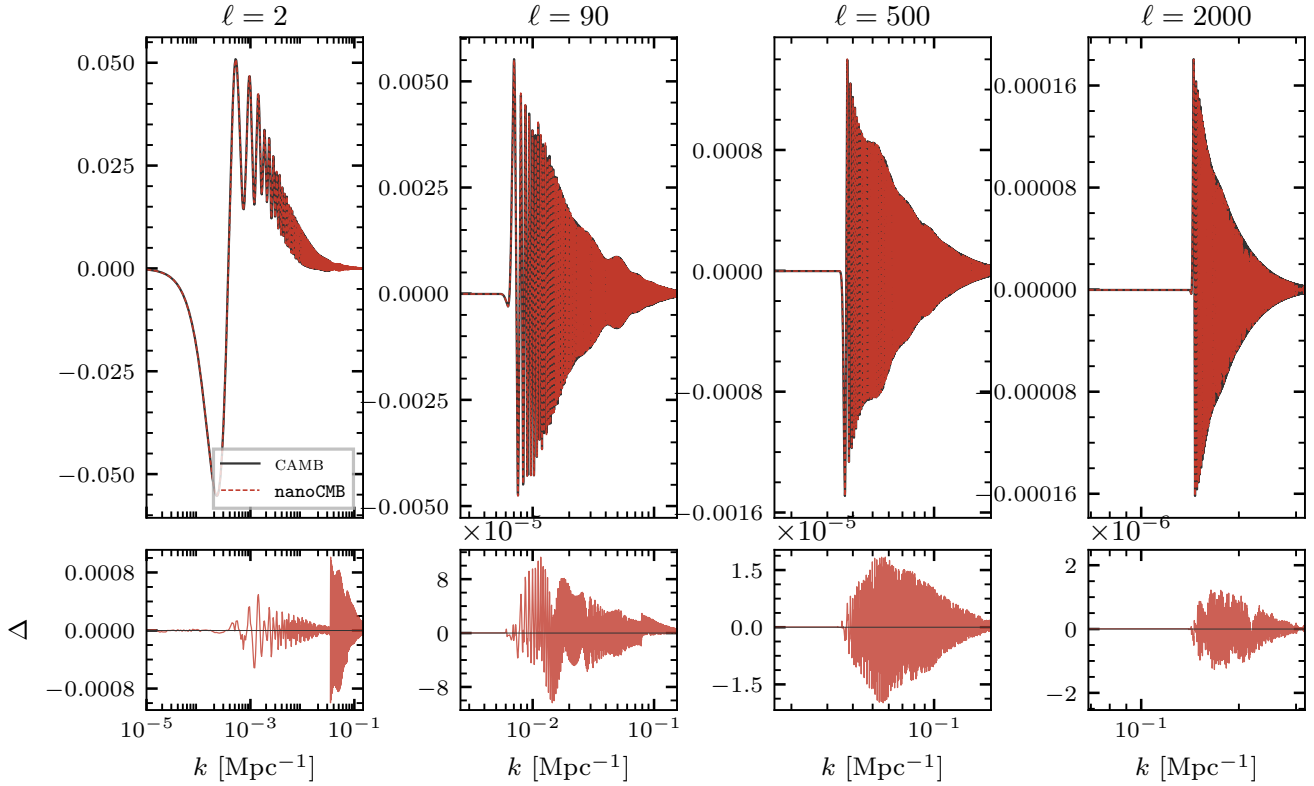


**Figure 4:** Temperature transfer functions  $\Delta_\ell^T(k)$  at four representative multipoles. Top panels show nanoCMB (red dashed) and CAMB (black solid); bottom panels show residuals.

## 5.5. Practical LOS integration

For each multipole  $\ell$ , we restrict the  $k$ -integration range to where  $j_\ell(k\chi)$  is non-negligible. Specifically, we integrate from  $k_{\text{lo}} = (\ell - 4\ell^{1/3})/\chi_{\text{max}}$  to  $k_{\text{hi}} = (\ell + 2500)/\chi_*$ , where  $\chi_* = \tau_0 - \tau_*$ . Outside this range, the Bessel function is either in the dead zone or has oscillated to negligible amplitude after averaging.

The LOS integrals for different  $\ell$  values are independent and are computed in parallel using Python’s `ThreadPool-Executor`. This provides near-linear speedup on multi-core machines since the computation is dominated by NumPy array operations that release the GIL.

Figure 4 compares the resulting temperature transfer functions  $\Delta_\ell^T(k)$  at four representative multipoles spanning  $\ell = 2$  to  $\ell = 2000$ . The oscillatory structure from the Bessel functions is well reproduced, and residuals are at the sub-percent level across the range of  $k$  that contributes significantly to  $C_\ell$ .

## 6. Power spectrum assembly

### 6.1. From transfer functions to angular power spectra

The angular power spectrum is

$$C_\ell^{XY} = 4\pi \int d(\ln k) \mathcal{P}(k) \Delta_\ell^X(k) \Delta_\ell^Y(k), \quad (43)$$

where  $\mathcal{P}(k) = A_s (k/k_0)^{n_s-1}$  is the dimensionless primordial power spectrum and  $X, Y \in \{T, E\}$ .

The conventional plotting quantity is  $\mathcal{D}_\ell = \ell(\ell + 1)C_\ell/(2\pi)$  in units of  $\mu\text{K}^2$ . For E-mode polarisation, an additional normalisation factor of  $[\ell(\ell - 1)(\ell + 1)(\ell + 2)]^{1/2}$  per transfer function accounts for the spin-2 nature of the polarisation field. For the cross-spectrum  $C_\ell^{TE}$ , this factor enters as the square root.

In code, the assembly is:

Listing 7: Power spectrum assembly.

```

1 Pk = A_s * (k_fine / k_pivot)**(n_s - 1.0)
2
3 Cl_TT, Cl_EE, Cl_TE = [np.trapezoid(Pk * d, lnk_fine, axis=1)
4     for d in (Delta_T**2, Delta_E**2, Delta_T * Delta_E)]
5
6 norm = 4.0 * np.pi * ells * (ells + 1) / (2.0 * np.pi)
7 ctnorm = (ells**2 - 1.0) * (ells + 2) * ells # E-mode factor
8 Cl_TT *= norm; Cl_EE *= norm * ctnorm
9 Cl_TE *= norm * np.sqrt(ctnorm)
    
```

### 6.2. Two-grid strategy

The source functions  $S(k, \tau)$  vary smoothly with  $k$  and can be accurately computed on a relatively coarse ODE grid. However, the transfer functions  $\Delta_\ell(k)$  oscillate rapidly (due to Bessel function ringing), and the  $C_\ell$  integrand  $|\Delta_\ell(k)|^2$  requires much finer  $k$ -sampling.

Our strategy is:

1. Solve the ODE system on 200 non-uniform  $k$ -modes (section 7).
2. Interpolate the source functions to a finer grid of 4000  $k$ -modes using Akima interpolation [2], which provides smooth results without the overshooting artefacts of cubic splines.
3. Perform the LOS integral and  $C_\ell$  integration on the fine grid.

This two-grid approach saves computation by a factor of  $\sim 10$  compared to solving the ODE on the fine grid directly.

### 6.3. Multipole sampling and interpolation

Rather than computing  $C_\ell$  at every integer  $\ell$  from 2 to 2500, we evaluate at a sparse set of  $\sim 100$  multipoles: every other  $\ell$  for  $\ell < 40$ , every 5th for  $40 \leq \ell < 200$ , and every 50th for  $\ell \geq 200$ . The full spectrum is then obtained by cubic spline interpolation in  $\ell$ . This is accurate because  $C_\ell$  varies smoothly with  $\ell$  (the rapid oscillations are in  $k$ , not  $\ell$ ).

## 7. Optimal non-uniform grids

### 7.1. Error equidistribution principle

The accuracy of the trapezoidal rule applied to  $\int f(x) dx$  on a non-uniform grid  $\{x_0, x_1, \dots, x_N\}$  is controlled by the local error  $e_i \sim h_i^3 |f''(x_i)|$ , where  $h_i = x_{i+1} - x_i$ . For a fixed total number of points  $N$ , the global error is minimised when the local errors are equidistributed across all intervals. This gives the optimal node density

$$\frac{dN}{dx} \propto |f''(x)|^{1/3}. \quad (44)$$

In practice, the integrand is not known a priori — its computation is the goal of the grid construction — so we cannot evaluate  $|f''|$  directly. The equidistribution principle nevertheless motivates the general strategy: construct a weight function  $w(x)$  that is large where the integrand is expected to have the most structure (large amplitude and rapid oscillation), then place nodes according to the cumulative distribution of  $w^{1/3}$ .

### 7.2. Wavenumber grid

A naïve choice is to distribute  $k$ -modes uniformly in  $\ln k$ , but this wastes points in regions where the integrand is smooth (low  $k$ ) while under-resolving the acoustic oscillations near the damping scale. A physically motivated weight function concentrates points where they matter most, achieving the same accuracy with significantly fewer modes (figure 5).

We construct two  $k$ -grids using the density (44):

*ODE grid* ( $N = 200$ ): The weight function captures the acoustic oscillation structure and damping of the source

functions:

$$w_{\text{ode}}(k) = \underbrace{\max\left(\frac{1}{r_s^2}, \frac{(k r_s)^2}{\tau_{\text{eq}}^2}\right)}_{\text{curvature}} \times \underbrace{k^{n_s+2}}_{\text{primordial}} \times \underbrace{e^{-(k/k_D)^2}}_{\text{Silk damping}}. \quad (45)$$

Each factor in this weight function has a direct physical motivation:

- *Silk damping*: The exponential  $e^{-(k/k_D)^2}$  reflects the suppression of the source functions by photon diffusion during recombination. Perturbation modes with  $k \gg k_D$  are exponentially damped, so there is no benefit in placing ODE grid points in this region.
- *Primordial weighting*: The factor  $k^{n_s+2}$  combines three contributions: the primordial power spectrum  $\mathcal{P}(k) \propto k^{n_s-1}$ , the logarithmic integration measure  $d \ln k$  (contributing one power of  $k$ ), and an additional factor of  $k^2$  reflecting the phase-space weighting of higher- $k$  modes in the  $C_\ell$  integral. Together, these determine the *amplitude* of the integrand at each  $k$  before accounting for oscillatory structure.
- *Curvature estimate*: The first factor determines where interpolation errors are largest by estimating how rapidly the source functions oscillate. Acoustic waves have period  $\sim \pi/r_s$  in  $k$ -space, so the second derivative of the oscillatory structure scales as  $(k r_s)^2$  — this is the one factor with a direct connection to  $|f''|$ . Dividing by  $\tau_{\text{eq}}^2$  normalises this against the timescale over which the transfer function envelope varies, giving a dimensionless measure of the curvature in the acoustic regime. The max with  $1/r_s^2$  provides a floor for super-horizon modes ( $k r_s \ll 1$ ), where there are no acoustic oscillations and the source functions are smooth, but some grid points are still needed to resolve the Sachs–Wolfe plateau. The transition between the two branches occurs near  $k \sim 1/\tau_{\text{eq}}$ , which corresponds approximately to the scale entering the horizon at matter–radiation equality — the boundary between modes that experienced acoustic oscillations and those that did not.

*$C_\ell$  grid* ( $N = 4000$ ): The  $C_\ell$  integrand  $\mathcal{P}(k) |\Delta_\ell(k)|^2$  oscillates rapidly in  $k$  due to Bessel function ringing, requiring much finer sampling than the ODE grid. The weight function accounts for the Bessel function windowing that selects  $k \approx \ell/\chi_*$  for each multipole:

$$w_{\text{cl}}(k) = \sum_{\ell} \exp\left[-\frac{(k - \ell/\chi_*)^2}{2(3\sigma_k)^2}\right] \times \max\left(\frac{1}{r_s^2}, \sigma_k^2\right) k^{n_s+2} e^{-(k/k_D)^2}, \quad (46)$$

where  $\sigma_k = 1/\Delta\tau_{\text{rec}}$  is the width of the visibility function in  $k$ -space. The Gaussian envelope centred on  $k = \ell/\chi_*$  approximates the Bessel window through which each multipole samples the source function; the sum over  $\sim 30$  geometrically spaced  $\ell$  values ensures that the grid resolves the integrand across the full multipole range. The curvature factor now uses  $\max(1/r_s^2, \sigma_k^2)$ : in the acoustic regime, the Bessel oscillation period  $\sim 1/\Delta\tau_{\text{rec}}$  sets the dominant curvature scale rather than the acoustic scale  $1/r_s$ , since the  $C_\ell$  integrand oscillates at the Bessel frequency, not the acoustic frequency.

Listing 8:  $k$ -grid density construction (ODE mode).

```

1 # Source-level damping: exp(-(k/k_D)^2)
2 primordial = k ** (params["n_s"] + 2)
3 damped = primordial * np.exp(-1.0 * (k / thermo["k_D"]) ** 2)
4
5 # Acoustic curvature
6 smooth_curv = (k * thermo["r_s"]) ** 2 / bg["tau_eq"] ** 2
7 raw_weight = np.maximum(1/thermo["r_s"]**2, smooth_curv) * damped
8
9 # Node density ~ weight^(1/3), with 0.5% floor
10 density = (raw_weight + 0.005 * np.max(raw_weight)) ** (1.0/3.0)
    
```

Figure 5 (top panels) shows the resulting node density  $dN/d \ln k$  for both grids compared to uniform  $\ln k$  spacing. The optimal grids concentrate points in the acoustic regime ( $k \sim 1/r_s$  to  $k \sim k_D$ ) while the uniform grid spreads them evenly. Figure 5 (bottom panel) demonstrates the payoff: the  $TT$  RMS residual versus CAMB as a function of the number of ODE  $k$ -modes, comparing the optimal and uniform grids. The optimal grid reaches  $\sim 0.1\%$  accuracy with  $\sim 150$  modes, whereas the uniform grid saturates at  $\sim 3\%$  even at  $N = 400$  because the evenly spread nodes cannot resolve the acoustic oscillation structure near the damping scale.

### 7.3. Conformal time grid

The  $\tau$ -grid ( $N = 1000$ ) must resolve three features: the narrow visibility peak at  $\tau_*$ , the broader acoustic source structure (width  $\sim r_s$ ), and the reionisation bump at  $\tau_{\text{reion}}$ :

$$w_\tau(\tau) = \frac{1}{\Delta\tau_{\text{rec}}^2} e^{-(\tau-\tau_*)^2/(2\Delta\tau_{\text{rec}}^2)} + \frac{k_{\text{max}}^2}{3} e^{-(\tau-\tau_*)^2/(2r_s^2)} + \frac{0.3}{\Delta\tau_{\text{reion}}^2} e^{-(\tau-\tau_{\text{reion}})^2/(2\Delta\tau_{\text{reion}}^2)}. \quad (47)$$

The node density is again  $\propto w^{1/3}$ , with a 0.5% floor. This concentrates points where the integrand has the most structure while maintaining adequate coverage elsewhere.

## 8. Validation

All comparisons in this section (and in the preceding figures) use CAMB [9] run with `AccuracyBoost=3`, configured with lensing disabled, no tensors, and massless neutrinos only, matching the nanoCMB assumptions. Figures use the Planck 2018 best-fit parameters listed in table 1; the multi-cosmology benchmark (section 8.2) spans  $\pm 3\sigma$  of the Planck posterior.

$\ell$ range	$TT$		$EE$	
	Mean ratio	Std	Mean ratio	Std
[2, 29]	0.9993	0.0008	1.0013	0.0099
[30, 499]	0.9996	0.0009	1.0005	0.0022
[500, 1999]	0.9998	0.0008	1.0003	0.0013
[2000, 2500]	0.9982	0.0005	0.9986	0.0020

Table 2

Accuracy summary for the fiducial cosmology: mean ratio and standard deviation of the nanoCMB/CAMB power spectra by multipole range. Sub-percent accuracy is achieved across the full range  $2 \leq \ell \leq 2500$ .

As shown in the preceding sections, the intermediate quantities agree well with CAMB: the Hubble parameter to  $\sim 10^{-4}$  (figure 1), the ionisation history and visibility function to  $\lesssim 0.5\%$  (figure 2), the perturbation variables to  $\sim 1\%$  at all  $k$ -modes tested (figure 3), and the transfer functions to sub-percent accuracy (figure 4).

### 8.1. Power spectra

Figures 6 and 7 show the  $TT$ ,  $EE$ , and  $TE$  angular power spectra from nanoCMB compared to CAMB for the fiducial parameters, with residual panels. Table 2 summarises the accuracy for this fiducial cosmology.

### 8.2. Multi-cosmology benchmark

To verify that the accuracy is not tuned to a single parameter set, we benchmark nanoCMB against CAMB across 50 flat  $\Lambda$ CDM cosmologies drawn from a Latin hypercube spanning  $\pm 3\sigma$  of the Planck 2018 posterior [1], varying  $\omega_b$ ,  $\omega_c$ ,  $h$ ,  $n_s$ ,  $\ln(10^{10} A_s)$ , and  $\tau_{\text{reion}}$  simultaneously. All 50 runs completed successfully.

Table 3 reports the RMS fractional residual

$$\left[ \left\langle \left( \frac{D_\ell^{\text{nano}}}{D_\ell^{\text{CAMB}}} - 1 \right)^2 \right\rangle_\ell \right]^{1/2}$$

within each multipole bin, summarised as the median and 95th percentile across the 50 cosmologies. For  $TT$ , the RMS residual is  $\lesssim 0.1\%$  at  $\ell < 2000$  and  $\sim 0.2\%$  in the highest bin, with negligible variation across cosmologies. For  $EE$  at  $\ell \geq 30$ , the RMS residual is 0.1–0.3%, comparable to  $TT$ .

The larger RMS for  $EE$  at  $\ell < 30$  reflects the very small amplitude of the reionisation bump ( $D_\ell^{EE} \lesssim 0.04 \mu\text{K}^2$ ), where even sub- $\mu\text{K}^2$  absolute differences produce sizeable fractional residuals. We do not report ratio-based statistics for  $C_\ell^{TE}$  because the cross-spectrum passes through zero at multiple multipoles, making fractional residuals ill-defined; the  $TE$  residuals visible in figure 7 are representative.

To put these residuals in context, CAMB's internal convergence at default accuracy is  $\sim 0.05$ – $0.1\%$  RMS when comparing `AccuracyBoost=1` to `AccuracyBoost=4`, comparable to the nanoCMB residuals. In other words, nanoCMB achieves accuracy comparable to CAMB at its default settings.

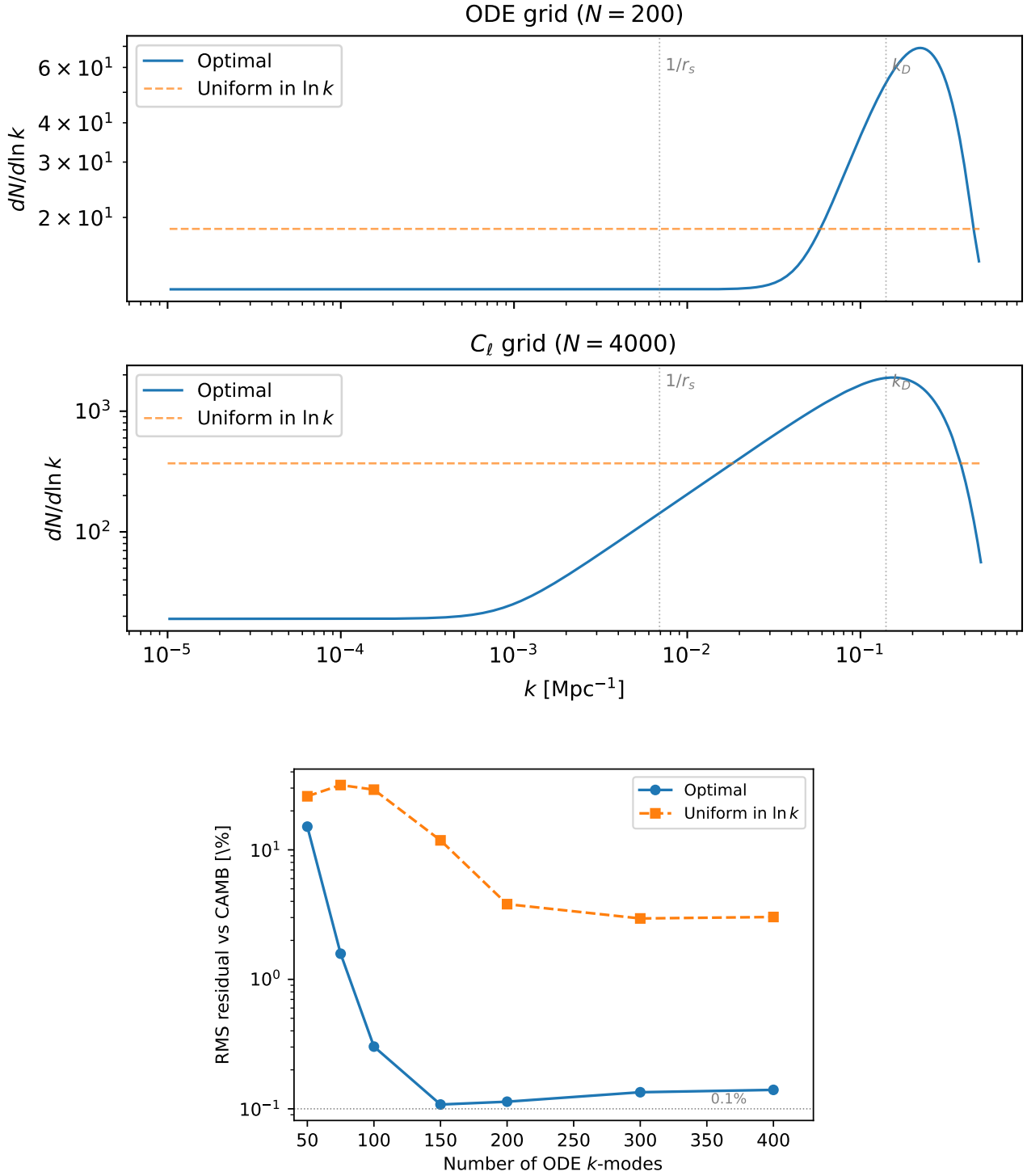


**Figure 5:** *Top panels:* Node density  $dN/d \ln k$  for the optimal (blue solid) and uniform-in- $\ln k$  (orange dashed) grids, for the ODE grid ( $N = 200$ , top) and  $C_\ell$  grid ( $N = 4000$ , bottom). Vertical dotted lines mark the acoustic scale  $1/r_s$  and the Silk damping scale  $k_D$ . *Bottom panel:*  $TT$  RMS residual versus CAMB as a function of the number of ODE  $k$ -modes, showing the convergence advantage of the optimal grid.

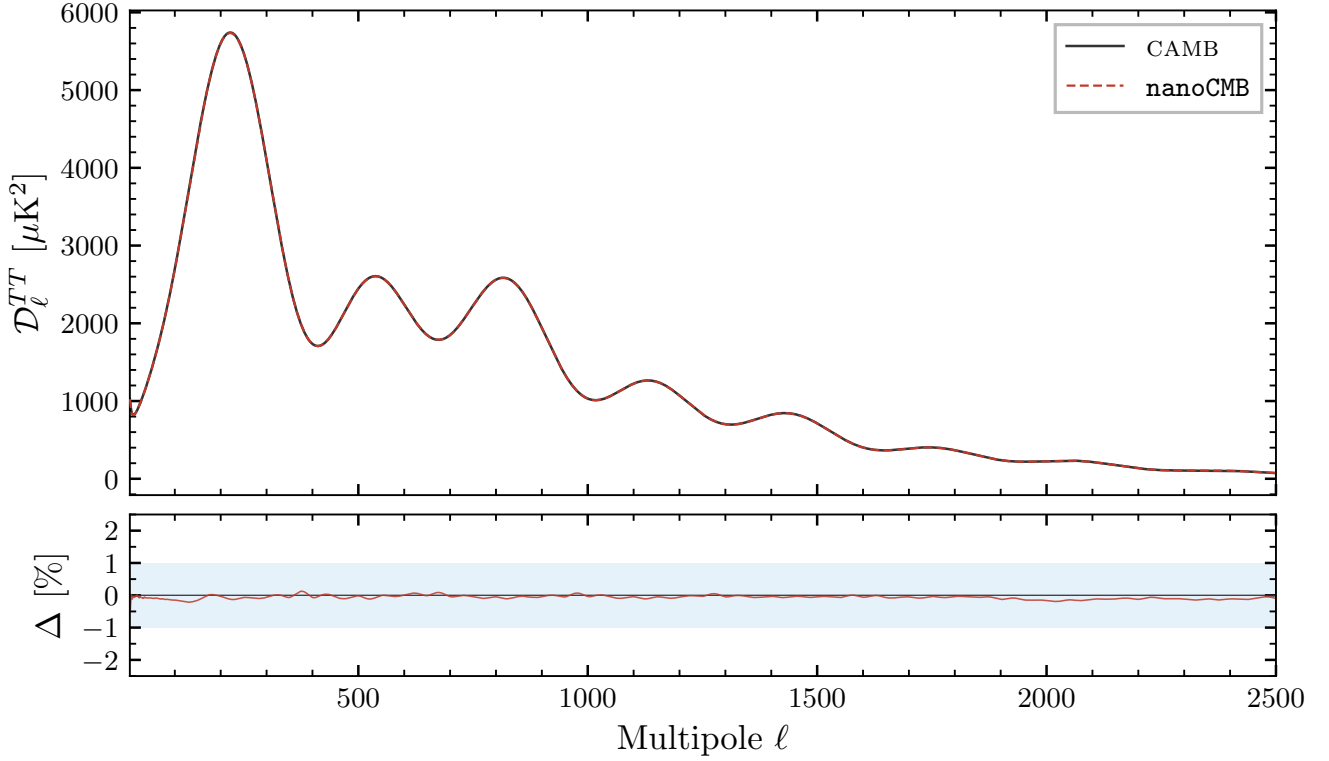


**Figure 6:** Temperature power spectrum  $D_{\ell}^{TT}$  from nanoCMB (red) compared to CAMB (black). The lower panel shows residuals as percentages, with the  $\pm 1\%$  band shaded.

$\ell$ range	$TT$		$EE$	
	Median	95th %ile	Median	95th %ile
[2, 29]	0.10%	0.12%	1.0% <sup>†</sup>	4.4% <sup>†</sup>
[30, 499]	0.09%	0.10%	0.22%	0.24%
[500, 1999]	0.08%	0.08%	0.14%	0.15%
[2000, 2500]	0.19%	0.21%	0.24%	0.29%

**Table 3**

Multi-cosmology benchmark: median and 95th-percentile of the RMS fractional residual in each multipole bin, across 50 cosmologies sampled over  $\pm 3\sigma$  of the Planck 2018 posterior. <sup>†</sup>Elevated at low  $\ell$  due to the small amplitude of the  $EE$  reionisation bump.

### 8.3. Timing

On an Apple M-series laptop (12 cores), the full calculation takes approximately 30 s without Numba, dominated by the perturbation evolution of 200  $k$ -modes parallelised across cores. With Numba JIT compilation enabled (optional), the runtime drops to  $\sim 10$  s. For comparison, CAMB at its default accuracy (`AccuracyBoost=1`) takes under a second for the same cosmology. The speed difference reflects the inherent overhead of a pure Python implementation relative to compiled Fortran; nanoCMB is not intended to compete on speed, but rather to provide a readable, self-contained reference implementation. The first run incurs an additional one-off cost to build the spherical Bessel function

lookup tables, which are then cached to disk and reused in subsequent runs.

## 9. Discussion and conclusions

We have presented nanoCMB, a pedagogical CMB power spectrum calculator that achieves sub-percent accuracy relative to CAMB in approximately 1400 lines of Python. The code is designed to be read alongside this paper, with each section corresponding to a clearly delineated block of the source code.

*Design philosophy.* Several deliberate choices keep the code readable:

- **Single file:** the entire calculation lives in `nanocmb.py`, with no package structure or build system.
- **Dictionary-based state:** background and thermodynamic quantities are passed as plain Python dictionaries, avoiding class hierarchies.
- **Minimal dependencies:** the only requirements are NumPy and SciPy (with optional Numba for acceleration).
- **Explicit over implicit:** every numerical choice (grid sizes, tolerances, truncation orders) is a visible constant or parameter, not hidden in a configuration file.

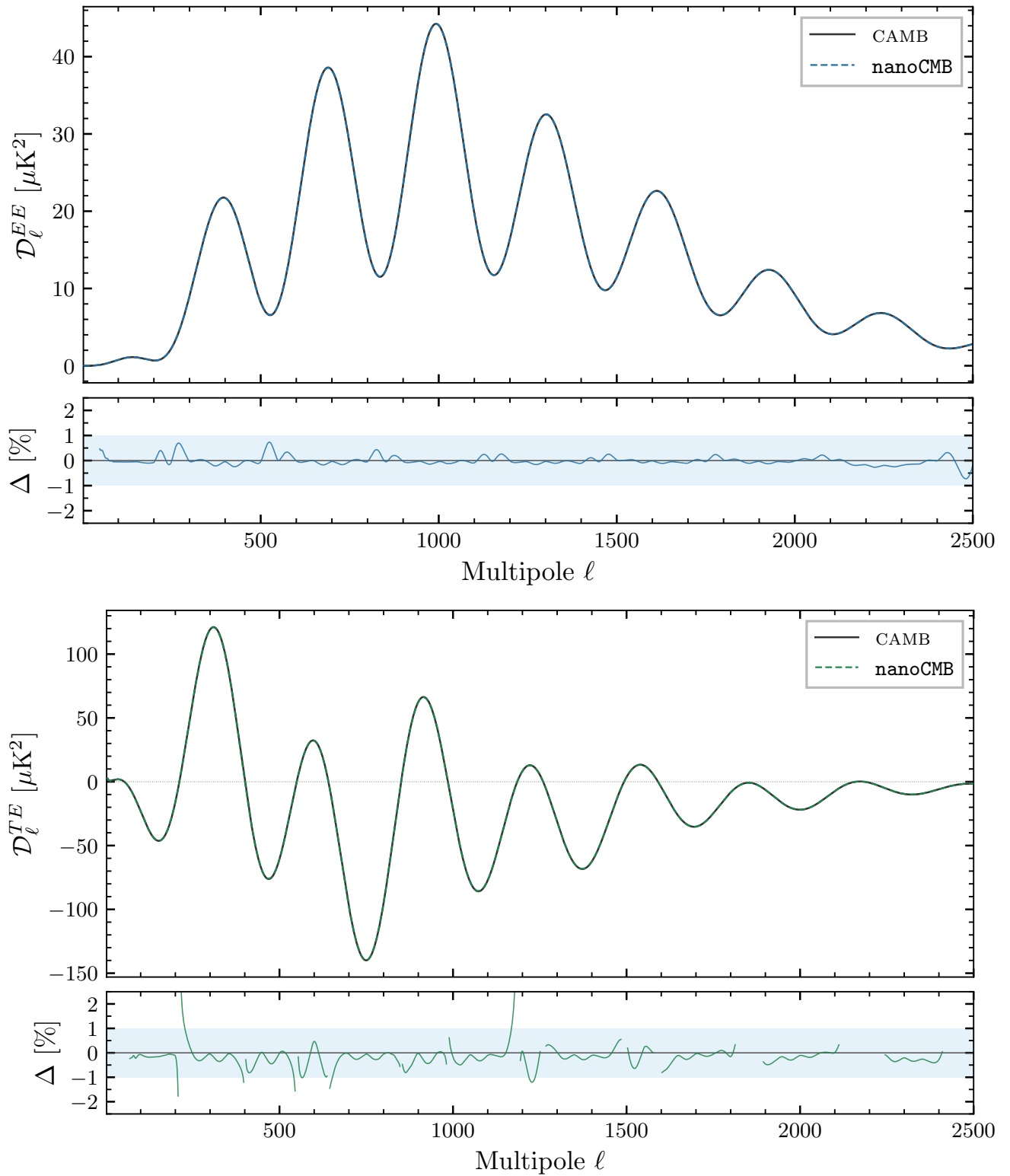


**Figure 7:** E-mode polarisation ( $D_{\ell}^{EE}$ , top) and temperature–polarisation cross-spectrum ( $D_{\ell}^{TE}$ , bottom) from nanoCMB compared to CAMB. Lower panels show residuals with the  $\pm 1\%$  band shaded.

Quantity	Symbol	Value
H ionisation	$L_{\text{H,ion}}$	$1.096788 \times 10^7 \text{ m}^{-1}$
H Lyman- $\alpha$	$L_{\text{H},\alpha}$	$8.225916 \times 10^6 \text{ m}^{-1}$
He I ionisation	$L_{\text{HeI,ion}}$	$1.983108 \times 10^7 \text{ m}^{-1}$
He II ionisation	$L_{\text{He2,ion}}$	$4.389089 \times 10^7 \text{ m}^{-1}$
He I $2^1S_0$	$L_{\text{He,2s}}$	$1.662774 \times 10^7 \text{ m}^{-1}$
He I $2^1P_1$	$L_{\text{He,2p}}$	$1.711349 \times 10^7 \text{ m}^{-1}$
H two-photon decay	$\Lambda_{2s \rightarrow 1s}$	$8.2246 \text{ s}^{-1}$
He I two-photon decay	$\Lambda_{\text{He}}$	$51.3 \text{ s}^{-1}$
He I $2^1P_1$ decay	$A_{2P,s}$	$1.798 \times 10^9 \text{ s}^{-1}$
He I $2^3P_1$ decay	$A_{2P,t}$	$177.58 \text{ s}^{-1}$
Thomson cross section	$\sigma_T$	$6.652 \times 10^{-29} \text{ m}^2$

**Table 4**

Atomic transition data used in the RECFAST recombination calculation.

*Limitations.* The current implementation omits several effects that are important for precision cosmology:

- Gravitational lensing of the CMB by large-scale structure, which smooths the acoustic peaks and generates B-mode polarisation.
- Tensor perturbations (gravitational waves), which contribute to B-modes at large scales.
- Massive neutrinos, which affect the matter power spectrum and CMB lensing.
- Spatial curvature ( $K \neq 0$ ).
- Non-standard dark energy ( $w \neq -1$ ).

*Possible extensions.* The modular structure makes extensions relatively straightforward. Gravitational lensing would require computing the lensing potential power spectrum  $C_\ell^{\phi\phi}$  and applying the lensing convolution. Tensor perturbations require a separate Boltzmann hierarchy for gravitational wave modes. Massive neutrinos require momentum-dependent distribution functions. Each of these extensions would add on the order of 100–200 lines, reusing the existing infrastructure (grids, Bessel tables, ODE solver).

## A. Atomic data

Table 4 lists the atomic constants used in the recombination calculation.

## B. State vector layout

The perturbation state vector  $\mathbf{y}$  is a flat array of  $N_{\text{var}} = 50$  elements, laid out as follows:

## Pipeline overview

Figure 8 shows a schematic overview of the nanoCMB computational pipeline.

Index	Variable	Symbol	Description
0	etak	$k\eta$	Metric
1	c1xc	$\delta_c$	CDM density
2	c1xb	$\delta_b$	Baryon density
3	vb	$v_b$	Baryon velocity
4–19	G[0..15]	$\Theta_0 \dots \Theta_{15}$	Photon temp.
20–33	POL[0..13]	$E_2 \dots E_{15}$	Photon pol.
34–49	R[0..15]	$\mathcal{N}_0 \dots \mathcal{N}_{15}$	Neutrino

**Table 5**

State vector layout for the Boltzmann hierarchy ODE system. Total: 50 variables.

## Acknowledgements

We thank Antony Lewis for developing and maintaining CAMB, which made the detailed validation in this work possible. The work of AM was supported by an STFC Consolidated Grant [Grant No. ST/X000672/1]. This work made use of CAMB [9] for validation, and NumPy [7] and SciPy [17] for numerical computation.

## Declaration of competing interest

The author declares that there are no known competing financial interests or personal relationships that could have appeared to influence the work reported in this paper.

## Data availability

The nanoCMB code, validation scripts, and all data needed to reproduce the figures in this paper are available at <https://github.com/adammoss/nanoCMB>.

## CRediT authorship contribution statement

**Adam Moss:** Conceptualization, Methodology, Software, Writing.

## References

- [1] Aghanim, N., et al. (Planck), 2020. Planck 2018 results. VI. Cosmological parameters. *Astron. Astrophys.* 641, A6. doi:10.1051/0004-6361/201833910, arXiv:1807.06209. [Erratum: *Astron. Astrophys.* 652, C4 (2021)].
- [2] Akima, H., 1970. A New Method of Interpolation and Smooth Curve Fitting Based on Local Procedures. *J. ACM* 17, 589–602. doi:10.1145/321607.321609.
- [3] Bertschinger, E., 1995. COSMICS: cosmological initial conditions and microwave anisotropy codes arXiv:astro-ph/9506070.
- [4] Blas, D., Lesgourgues, J., Tram, T., 2011. The Cosmic Linear Anisotropy Solving System (CLASS) II: Approximation schemes. *JCAP* 07, 034. doi:10.1088/1475-7516/2011/07/034, arXiv:1104.2933.
- [5] Callin, P., 2006. How to calculate the CMB spectrum arXiv:astro-ph/0606683.
- [6] Dodelson, S., Schmidt, F., 2020. *Modern Cosmology*. Academic Press. doi:10.1016/C2017-0-01943-2.
- [7] Harris, C.R., et al., 2020. Array programming with NumPy. *Nature* 585, 357–362. doi:10.1038/s41586-020-2649-2, arXiv:2006.10256.
- [8] Hummer, D.G., Storey, P.J., 1998. Recombination of helium-like ions — I. Photoionization cross-sections and total recombination and

- cooling coefficients for atomic helium. *Mon. Not. Roy. Astron. Soc.* 297, 1073–1078. doi:10.1046/j.1365-8711.1998.01596.x.
- [9] Lewis, A., Challinor, A., Lasenby, A., 2000. Efficient computation of CMB anisotropies in closed FRW models. *Astrophys. J.* 538, 473–476. doi:10.1086/309179, arXiv:astro-ph/9911177.
- [10] Ma, C.P., Bertschinger, E., 1995. Cosmological perturbation theory in the synchronous and conformal Newtonian gauges. *Astrophys. J.* 455, 7–25. doi:10.1086/176550, arXiv:astro-ph/9506072.
- [11] Peebles, P.J.E., 1968. Recombination of the Primeval Plasma. *Astrophys. J.* 153, 1. doi:10.1086/149628.
- [12] Pequignot, D., Petitjean, P., Boisson, C., 1991. Total and effective radiative recombination coefficients. *Astron. Astrophys.* 251, 680–688. doi:10.1051/0004-6361/19910127.
- [13] Scott, D., Moss, A., 2009. Matter temperature after cosmological recombination. *Mon. Not. Roy. Astron. Soc.* 397, 445–446. doi:10.1111/j.1365-2966.2009.14939.x, arXiv:0902.3438.
- [14] Seager, S., Sasselov, D.D., Scott, D., 1999. A new calculation of the recombination epoch. *Astrophys. J. Lett.* 523, L1–L5. doi:10.1086/312250, arXiv:astro-ph/9909275.
- [15] Seager, S., Sasselov, D.D., Scott, D., 2000. How exactly did the universe become neutral? *Astrophys. J. Suppl.* 128, 407–430. doi:10.1086/313388, arXiv:astro-ph/9912182.
- [16] Seljak, U., Zaldarriaga, M., 1996. A Line of sight integration approach to cosmic microwave background anisotropies. *Astrophys. J.* 469, 437–444. doi:10.1086/177793, arXiv:astro-ph/9603033.
- [17] Virtanen, P., et al., 2020. SciPy 1.0–Fundamental Algorithms for Scientific Computing in Python. *Nature Meth.* 17, 261. doi:10.1038/s41592-019-0686-2, arXiv:1907.10121.
- [18] Wong, W.Y., Moss, A., Scott, D., 2008. How well do we understand cosmological recombination? *Mon. Not. Roy. Astron. Soc.* 386, 1023–1028. doi:10.1111/j.1365-2966.2008.13092.x, arXiv:0711.1357.
- [19] Zel’dovich, Y.B., Kurt, V.G., Syunyaev, R.A., 1968. Recombination of Hydrogen in the Hot Model of the Universe. *Zh. Eksp. Teor. Fiz.* 55, 278. [*Sov. Phys. JETP* 28 (1969) 146].

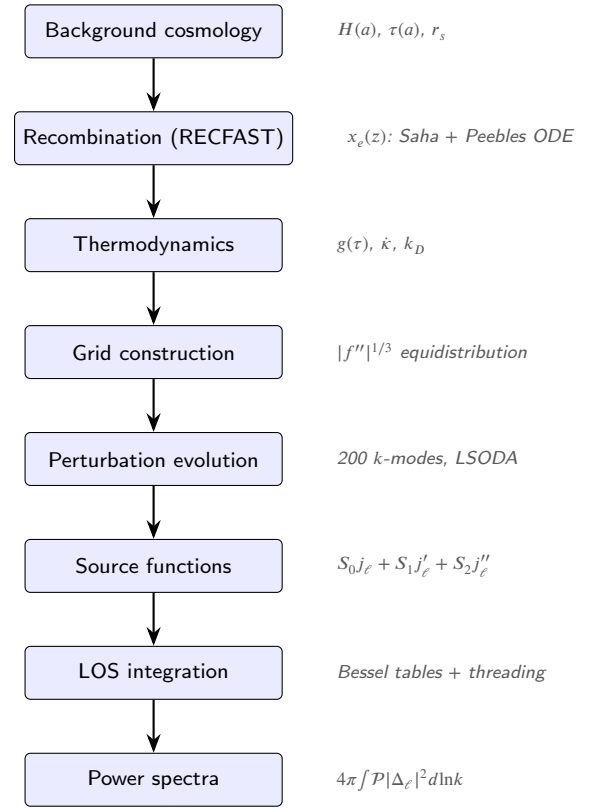


**Figure 8:** Schematic of the nanoCMB computational pipeline, from cosmological parameters to angular power spectra.